Analytica Chimica Acta 1124 (2020) 60–70

Contents lists available at ScienceDirect

Analytica Chimica Acta

journal homepage: www.elsevier.com/locate/aca

Capacitively coupled contactless conductivity detection for microfluidic capillary isoelectric focusing

Minh Khang Chau [a], Nebiyu Getachew Arega [a], Nguyen Anh Nhung Tran [b], Jin Song [a], Sangmin Lee [b], Jintae Kim [c], Minsub Chung [b], Dohyun Kim [a, d, *]

[a] Department of Mechanical Engineering, Myongji University, Yongin-si, Gyeonggi-do, 17508, South Korea
[b] Department of Chemical Engineering, Hongik University, Mapo-gu, Seoul, 04066, South Korea
[c] Department of Electrical Engineering, Konkuk University, Gwangjin-gu, Seoul, 05029, South Korea
[d] Natural Science Research Institute, Myongji University, Yongin-si, Gyeonggi-do, 17508, South Korea

HIGHLIGHTS

- First μCIEF-C4D (microfluidic capillary isoelectric focusing with capacitively coupled contactless conductivity detection).
- A mechanism study and a rational assay design for the μCIEF-C4D of protein were performed using numerical simulation.
- μCIEF-C4D assay was experimentally verified using conductivity and fluorescence protein co-detection.
- Label-free protein detection with notable performance: 10 nM LOD, up to 30 μM detection range, and 2.53% RSD reproducibility.
- Multianalyte protein separation and detection with resolving power of 0.25 pH unit and 12-min assay time.

GRAPHICAL ABSTRACT

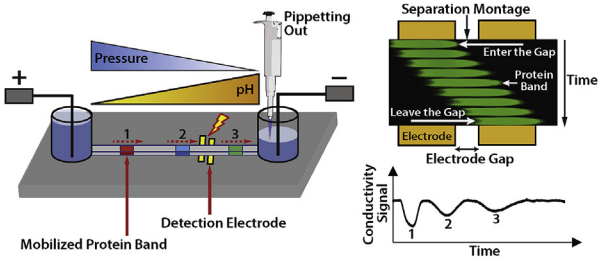

Contactless Conductivity Detection of Pressure-Mobilized Protein Bands

ARTICLE INFO

Article history:
Received 19 November 2019
Received in revised form
25 March 2020
Accepted 9 May 2020
Available online 13 May 2020

Keywords:
Microfluidic isoelectric focusing
Protein analysis
Protein separation
Capacitively coupled contactless conductivity detection
Label-free detection
Numerical simulation

ABSTRACT

We report capacitively coupled contactless conductivity detection (C4D) of proteins separated by microfluidic capillary isoelectric focusing (μCIEF). To elucidate the evolution of negative conductivity peaks during focusing and seek IEF conditions for sensitive conductivity detection, numerical simulation was performed using a model protein GFP (green fluorescence protein) and hypothetical carrier ampholytes (CAs). C4D was successfully applied to the μCIEF by optimizing assay conditions using a simple and effective pressure-mobilization approach. The conductivity and fluorescence signals of a focused GFP band were co-detected, confirming that the obtained negative C4D peak could be attributed to the actual protein, not the non-uniform background conductivity profile of the focused CAs. GFP concentrations of 10 nM–30 μM was quantified with a detection limit of 10 nM. Finally, the resolving power was analyzed by separating a mixture of R-phycoerythrin (p*I* 5.01), GFP-F64L (p*I* 5.48), and RK-GFP (p*I* 6.02). The conductivities of the three separated fluorescence proteins were measured with average

* Corresponding author. Department of Mechanical Engineering, Myongji University, Yongin-si, Gyeonggi-do, 17508, South Korea.
E-mail address: dohyun.kim@mju.ac.kr (D. Kim).

https://doi.org/10.1016/j.aca.2020.05.028

separation resolution of 2.06. We expect the newly developed label-free μCIEF-C4D technique to be widely adopted as a portable, electronics-only protein-analysis tool.

1. Introduction

Isoelectric focusing (IEF) is an electrophoresis method used for separating and enriching zwitterionic molecules (e.g., proteins and peptides) based on isoelectric point (p*I*). With its typically shorter separation length and smaller channel diameter compared to those of macroscale IEF, microfluidic IEF (μIEF) allows for reduced sample and reagent consumption [1,2], shorter analysis time [3], and smaller power consumption without sacrificing resolving power [2]. Various IEF methods have been translated into the microfluidic format, including gel IEF (μGIEF) [4,5], capillary IEF (μCIEF) [6,7], free-flow IEF (μFFIEF) [8,9], and immobilized pH gradient (μIPG) [10,11]. Multi-dimensional separation (e.g., subsequent size-based separation in the 2nd dimension) can also be performed on chip [4,12,13]. The μIEF has been used for proteomic research [14,15] and disease-diagnostics applications [16,17]. It is challenging to use ELISA for protein-isoform analysis since there is no specific antibody for protein isoforms [18], but the analysis of prostate-specific antigen (PSA) isoforms by μIEF can assist prostate cancer diagnosis [16].

Optical detection is commonly used in μIEF. Fluorescence detection has been widely used because of high sensitivity. Laser-induced fluorescence (LIF) detection achieved a limit of detection (LOD) as low as 0.7 nM [19]. However, time-consuming fluorescence labeling was required. In addition, fluorescence labeling can result in both protein heterogeneity [20] and increased hydrophobicity [21]. UV detection does not require labeling but exhibits a limited sensitivity (LOD on the order of ~1 μM) [22]. Both techniques require bulky and complex optical instrumentation, which may not be amenable to highly portable analytical instruments.

Capacitively coupled contactless conductivity detection (C4D) relies on simple yet universal conductometry [23,24] for charged species such as inorganic ions [25] and organic molecules including amino acids [26], peptides [27], proteins [28], and nucleic acids [29]. It has been commonly used in conjunction with electrokinetic sepataion methods including zone electrophoresis and isotachophoresis. Analytes in the background electrolyte are capacitively coupled with electrodes, contacting the outer surface of a microfluidic channel. Without direct electrolyte contact, unwanted side reactions such as electrolysis [30] and interference from high separation voltage are precluded [31]. Moreover, compared to "contact" conductivity methods, the microfabrication process is simpler as the electrodes are not required to be placed inside a microchannel [32]. Thus electronics-based C4D may be better suited for miniaturized analytical systems compared to optical detection methods. Portable analytical instruments based on C4D have undergone significant development recently [33,34]. A major drawback of the C4D method may be the high LOD inherent to weak capacitive coupling (~10^{-13} F) [35] through a thick dielectric layer [36]. Significant efforts have been devoted to improving the LOD including maximizing coupling capacitance [37] and combination with enrichment techniques [38,39].

Herein, we seek to combine the convenience of C4D and the performance of microfluidic-format capillary IEF (μCIEF) offering advantages of sensitivity, resolution, and throughput [40]. Despite a large body of the literature on C4D combined with microchip electrophoresis, *to the best of our knowledge,* the application of C4D in μCIEF has not been reported [41,42]. The focusing (i.e., enrichment) capabilities of μCIEF seem appropriate for C4D to improve the inferior LOD. However, as the charge and mobility of a focused protein decrease significantly while migrating toward its p*I*, so does the conductivity. For the same reason, the conductivity of carrier ampholytes (CAs) also significantly decreases [43]. Therefore, the detection of a protein conductivity peak can be quite challenging. Moreover, the conductivity profiles of focused CAs are not generally uniform [44] and have shown peak-like features irrelevant to focused analytes [45], further hindering distinct peak detection. Therefore, we performed numerical simulation for IEF using a model protein GFP (green fluorescence protein) and hypothetical CAs to determine the spatial and temporal distributions of all species and the associated conductivity. The simulation results help elucidate the evolution of protein conductivity peaks and examine the feasibility of conductivity detection of a focused protein. Relationships between conductivity and major protein physicochemical parameters including mobility, charge, and concentration were examined to find conditions suitable for sensitive conductivity detection.

C4D detection often relies on single-point detection, necessitating a mobilization step. Hydraulic or pressure mobilization [46] is initiated by applying a positive or negative pressure, and constant flow rate yields a linear relationship between the retention time and analyte p*I* [47]. Chemical mobilization [48] can be achieved by disrupting the pH gradient, for example by replacing the catholyte with an acid or the anolyte with a base [49]. Chemical mobilization may provide better resolution [1] but mobilizing ions (i.e., Na^+) can disturb the conductivity of the separation medium [48], posing a challenge for the conductivity detection of focused proteins. Herein, we developed a simple and effective pressure mobilization method by aspiring a small portion of the catholyte solution, creating a hydrostatic pressure difference between the anolyte and catholyte reservoirs. Meanwhile, the electric field was increased to minimize band dispersion [50]. As CA species in a high pH range are mixed with the catholyte solution during pressure mobilization, the stability of the gradient was experimentally examined.

Because of the aforementioned analytical challenges, the μCIEF-C4D assay was tested by co-detecting GFP using C4D and fluorescence imaging. Assay performance was thoroughly characterized, and multi-species protein determination was demonstrated along with resolving capability. Finally, the performance of C4D was compared with that of fluorescence detection.

2. Experimental

2.1. Chemicals and reagents

All chemicals were of reagent grade. Solutions were prepared using 18.2 MΩ·cm deionized water (Young In Chromass, Anyang, South Korea). Carrier ampholytes (Pharmalytes pH 4–6.5, product number #P1772), *2-hydroxyethyl* cellulose (HEC; molecular mass ~90 kDa, #434965, 0.15 Pa s at 5% m/m in water), 3-[(3-*cholamidopropyl*) *dimethylammonio*]-1-*propanesulfonate* hydrate (CHAPS; #C9426), fluorescent IEF markers p*I* 4.0 (#89827), 6.2 (#17958), 6.6 (#73376), and phosphoric acid (H_3PO_4; #1610761, 70 mM) were purchased from Sigma-Aldrich (St. Louis, MO, USA).

Sodium hydroxide (NaOH; #7574-3700, 0.1 M) was obtained from Daejung Chemicals and Metals (Siheung, South Korea). Two variants of *aequorea victoria* green fluorescent protein (avGFP) were used for the μCIEF-C4D assay. An avGFP-F64L mutant produced in the lab was used for the μCIEF-C4D confirmation experiment and assay-performance characterization. RK-GFP with high p*I* (6.02) was designed by adding basic amino acids (RKRKR) to the C-terminal end and a six-histidine tag to the N-terminal end of avGFP. Fluorescence protein R-phycoerythrin (R-PE; ~240 kDa, #P801) was obtained from Molecular Probes (Eugene, OR, USA). RK-GFP and R-PE were used for multispecies-detection assessment. The detailed description of GFP expression is provided in Section S.1, Supplementary Data (S.D.).

2.2. Microfluidic chip

A cyclic-olefin-copolymer (COC) chip in a microscope-slide format (72 mm × 28 mm) containing eight replicates of a straight channel (100 μm × 100 μm × 18 mm) and two terminal reservoirs was purchased from Microfluidic ChipShop (#01-0181-0157-02, Jena, Germany). The chip was chosen because of its exceptionally thin cover lid (140 μm) for effective capacitive coupling and ample reservoir volume (60 μL) for easy pressure mobilization. The chip was diced to yield eight replicate devices using a CO_2-laser cutter (Mini 18, Epilog Laser, Golden, CO, USA) with the following cutting parameters: speed, 2%; power, 6%; and frequency, 5000 Hz.

2.3. Instrumentation and data acquisition

A C4D detector (ER225) was used with a C4D headstage (ET121) and chromatography software (PowerChrom), all from eDAQ (Denistone, Australia). The headstage contained two antiparallel [51] gold-coated copper-strip electrodes (1 mm × 4 mm each, separated by 0.5 mm) placed perpendicular to the microchannel. For effective capacitive coupling, the microfluidic chip was tightly pressed to the electrodes using a custom-made Plexiglas clamp. An excitation signal for C4D detection was determined for the maximum signal-to-noise ratio using the PowerChrom software and a test solution (2% (v/v) CA, 4% (m/v) HEC, and 5% (m/v) CHAPS): amplitude 200 V and frequency 300 kHz. A separation voltage for IEF was applied using a pair of platinum-wire electrodes (Nilaco, Tokyo, Japan) connected to a high-voltage sequencer HVS448LC (LabSmith, Livermore, CA, USA). Protein migration during the separation and mobilization steps was observed using an epi-fluorescence upright microscope BX50 (Olympus, Tokyo, Japan) equipped with a Peltier-cooled CCD camera CoolSNAP HQ^2 (Photometrics, Tucson, AZ, USA) and an automated LED light source ($pE300^{ultra}$, CoolLED, River Way, Andover, UK). The images were collected and stitched, if necessary, using MetaMorph software (Molecular Devices, Sunnyvale, CA, USA). Image capture was achieved with a 4 × objective lens (UPlanFLN, Olympus, Tokyo, Japan), 4 × 4 binning, 100-ms exposure time, and 1 × amplifier gain. The image was background-subtracted (50-pixel rolling-ball radius) and analyzed using ImageJ (NIH, Bethesda, MD, USA) to obtain the electropherograms. Peak properties, including position, width, height, and area, were obtained using the Peak Analyzer tool in OriginPro 2018 (OriginLab, Northampton, MA, USA).

2.4. Optimization of the mobilization conditions

The mobilization conditions for the μCIEF-C4D assay were optimized using fluorescence imaging to minimize peak broadening for high separation resolution and maximize mobilization speed for rapid C4D measurement. This included optimization of separation-medium viscosity (i.e., HEC concentration). GFP (10 μM) was added in a separation medium consisting of 2% (v/v) CA, 5% (m/v) CHAPS, and 3–5% HEC. Before IEF, the microchannel was thoroughly cleaned using 0.1 M NaOH for 10 min and subsequently rinsed with DI water for 10 min. To minimize electroosmotic flow (EOF) and prevent non-specific protein adsorption on the COC surface, HEC was chosen as a dynamic coating agent [52]. The separation medium was loaded into the channel. Subsequently, the anolyte reservoir was filled with 35 mM H_3PO_4 (pH 1.74) + 2% HEC, while the catholyte reservoir was filled with 35 mM sodium hydroxide (pH 12.43) + 2% HEC. An electric field of 55.6 V/cm was applied for focusing. After focusing, the GFP band was mobilized in the cathode direction by removing 10-μL catholyte from the cathode reservoir using a micropipette. Because the reservoir can hold 60 μL, only 10 μL was removed to ensure sufficient catholyte remained to maintain a stable pH, as the high-pH end is especially prone to carbonate contamination and pH shift [53]. The height difference between the anolyte and catholyte levels was 1.20 mm after removing 10 μL, which generated the velocity of mobilized protein band determined to be ~0.375 mm/min. Migration images of the GFP band were captured at 30-s intervals for 4 min. The peak width was measured to determine peak broadening at different HEC concentrations. The peak-migration speed was also measured using peak-location changes during the given mobilization time.

2.5. Study of pH-gradient stability

The stability of the pH gradient during pressure mobilization was studied using fluorescence imaging. The "standard separation medium" consisted of 2% CA, 4% HEC, and 5% CHAPS. The p*I* markers (p*I* values of 4.0 and 6.2; 0.05 mg/mL each) were added to the medium. The experimental process and image capture condition were the same as the optimization step of the mobilization conditions (Section 2.4). The position of the p*I* marker bands at different times was determined using OriginPro. The slope of the pH gradient indicated by the two p*I* markers was determined as a function of time to characterize the temporal stability of the pH gradient.

2.6. Determination of protein pI values

The p*I* values of the fluorescence proteins were determined using the μCIEF assay and fluorescence imaging. RK-GFP (1 μM), GFP-F64L (1 μM), and R-PE (500 nM) were added to the same separation medium. The separation electric field was identical. A linear pH gradient between 4.0 and 6.6 was obtained based on the location of the two p*I* markers, and the protein p*I* values were determined using the pH gradient.

2.7. μCIEF-C4D assay procedures

The μCIEF-C4D assay procedure is illustrated in Fig. 1, which is similar to the optimization step of the mobilization conditions (Section 2.4). Step 1: proteins are added to the separation medium. The medium was subsequently loaded into the microchannel precoated with HEC. The reservoirs were filled with catholyte and anolyte solutions. The C4D detector was turned on at least ~60 min before running IEF to stabilize the baseline signal; Step 2: an electric field (55.6 V/cm) was applied to establish a pH gradient and focus the loaded proteins at their p*I*s; Step 3: once the proteins were focused, as confirmed by fluorescence imaging, the electric field was increased to 83.3 V/cm to minimize dispersion, and the proteins were pressure-mobilized to the detection point (i.e., C4D electrodes) by removing 10 μL of the catholyte. The conductivity data and fluorescence signals of the mobilized proteins were measured concurrently. Both data were analyzed using ImageJ and

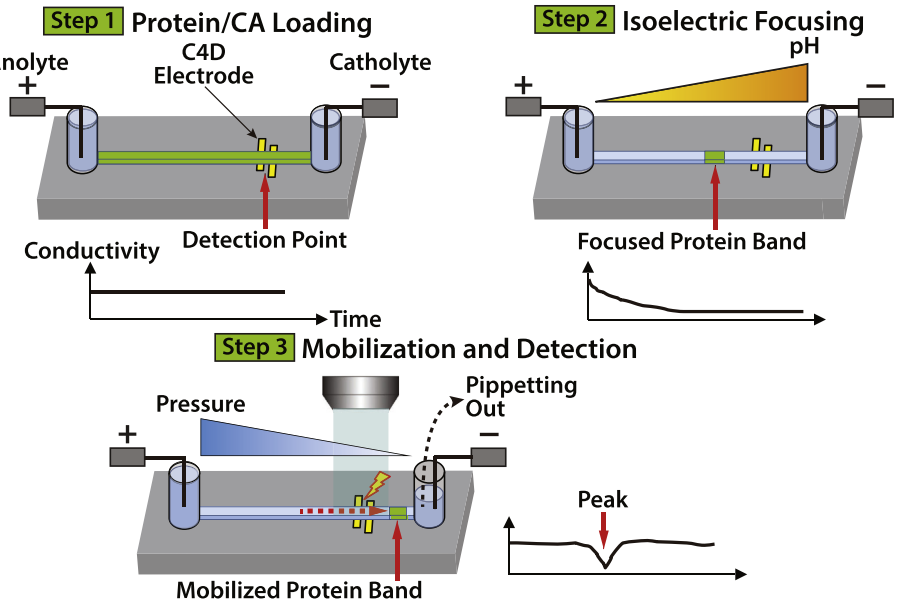

Fig. 1. The μCIEF-C4D assay procedure. Step 1: loading of catholyte and anolyte solutions, and the standard separation medium containing proteins after surface treatment of the microchannel; Step 2: isoelectric separation and focusing of the proteins by applying an electric field; and Step 3: mobilization to the detection point using hydrostatic pressure differences and subsequent C4D detection. Protein separation and mobilization were monitored using a fluorescence microscope to confirm the protein C4D signal and facilitate the assay.

OriginPro for μCIEF-C4D assay confirmation. The conductivity data were used for protein quantitation and multi-analyte detection, while the fluorescence imaging was used to validate the μCIEF-C4D assay and assist the assay procedure.

2.8. Quantitative and multi-analyte detection for μCIEF-C4D

To investigate the detection range and LOD of the developed assay, GFP-F64L ranging from 10 nM to 35 μM in the same standard separation medium was focused, and the resulting conductivity was measured. The obtained conductivity signals were imported to OriginPro to determine the peak heights. The interpolation method with a spline curve (3rd order polynomials) in OriginPro was used for baseline correction. For multiple-protein analysis, a mixture of fluorescent proteins RK-GFP, GFP-F64L, and R-PE was separated and detected using our μCIEF-C4D assay. The separation resolution (R_s) between peaks was calculated using the following formula [3]: $R_s = 2(x_2 - x_1)/(w_2 + w_1)$, where x_1 and x_2 are the locations and w_1 and w_2 are the widths of the two peaks. Based on the determined p*I* values and R_s between the protein C4D signals, the IEF resolution (ΔpH) of the μCIEF-C4D assay was estimated. Further details regarding the resolution calculation are provided in Section S.8 of the S.D.

2.9. Numerical simulation of IEF

Dynamic IEF simulations were conducted using open-source electrophoresis-simulation software Simul5 written by Gas et al. [54]. Simulation parameters including channel dimension, buffers, analytes, time steps, and mesh size were chosen to mimic the experimental conditions as closely as possible. A channel dimension of 18-mm length and 50-μm diameter was used for simulation. The cross-sectional area of the catholyte and anolyte reservoirs was 100 times larger than that of the channel to account for the significantly larger reservoir volumes (60 μL), compared to that of the channel (0.18 μL). The channel was divided into 3000 segments of equal length, and the time step for simulation was automatically adjusted by the software (~15 ms at the final time step). A separation electric field of 55.6 V/cm was used. Hypothetical diprotic CAs (total of 31 species) of concentration of 0.516 mM covered the pH range 4–7. The pH range was 0.5 pH units broader than that of the actual CAs (i.e., pH 4–6.5) to minimize distortion of the conductivity peaks of the target proteins near p*I* = 5.94, which was caused by non-uniform conductivity profile at the alkaline end of the pH range. The CA p*I* values uniformly span the given pH range with Δp*I* = 0.1. For all CAs, Δp*K* was 1, and electrophoretic mobility was 30×10^{-9} $m^2/V \cdot s$ [55]. The anolyte and catholyte were 35 mM H_3PO_4 and 35 mM NaOH, respectively. For the model protein GFP, the amino-acid sequence of avGFP (Section S.3.2) and base mobility (i.e., singly-charged state) of 1.96×10^{-9} $m^2/V \cdot s$ were used. The molecular mass and p*I* of avGFP used in simulations and the F64L variant used in experiments are almost identical (<0.1% difference in p*I* and <0.01% difference in molecular mass, see Section S.1). Simul5 automatically calculates mobility at different pH values using a user-defined formula so that GFP, situated farther from its p*I* in a pH gradient, has a higher charge and consequently larger mobility. The S.D. (Section S.3) provides further details regarding all simulation parameters. The mechanisms underlying the generation of a notable negative conductivity peak from protein focusing were studied, and a first-degree idea to improve the detection sensitivity was proposed from the simulation outputs, namely the spatial and temporal distributions of (1) CAs, proteins, catholyte, and anolyte; (2) pH; (3) electric field; (4) conductivity; and (5) current.

3. Results and discussion

3.1. Numerical simulation results and interpretation

The numerical simulation was performed to understand the mechanisms of conductivity-peak evolution and propose a first-degree solution for improving detection sensitivity. The spatial and temporal distribution of CAs and pH are shown in Fig. 2a and b, respectively. The time-dependent focusing of GFP and the evolution

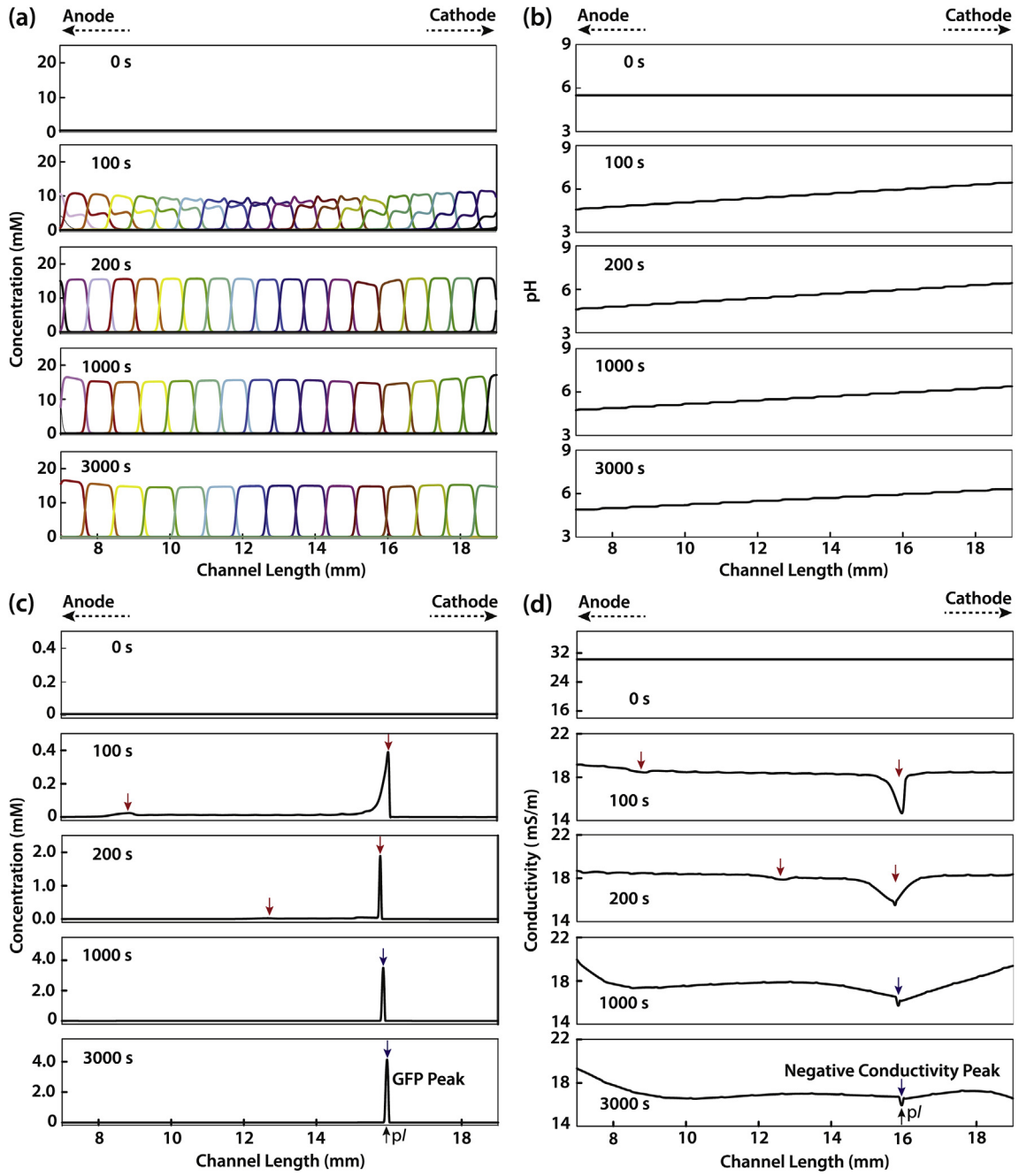

Fig. 2. IEF simulation results in a microfluidic channel using Simul5 software at 100, 200, 1000, and 3000 s after the onset. (a) 31 CA constituents for the pH 4–7 range (the CA concentration profiles are colored for differentiation). (b) Spatial distribution of pH 4–7. (c) Concentration profile of GFP. Two peaks from both ends (red arrows) of the initially-dispersed GFP migrate toward its p*I* and merge into a single peak (blue color). The focusing position of the GFP (p*I* = ~5.94) was observed at 15.947 mm. (d) Conductivity profile. Negative conductivity peaks (red arrow) coinciding with the two GFP peaks eventually merged into a single negative peak (blue arrow). (For interpretation of the references to color in this figure legend, the reader is referred to the Web version of this article.)

of its conductivity profile are shown in Fig. 2c and d, respectively. At the onset of the simulation (t = 0 min), the CA concentrations (Fig. 2a) and GFP concentration (Fig. 2c) were uniform (0.5162 mM for the CAs and 10 μM for GFP) throughout the microchannel along with the conductivity (30.26 mS/cm, Fig. 2d). However, in the anolyte- and catholyte-reservoir regions, the conductivity was much higher (not shown). A sigmoid-like smooth transition of all species from the reservoirs to the microchannel was used (not shown) as the initial condition to improve the convergence of the numerical simulation.

Two peaks (red arrows) were formed at the two ends of the initially dispersed GFP (Fig. 2c). The GFP stacks because effective mobility progressively reduces as it approaches its p*I* point. The two peaks were finally merged into a single, enriched peak at its p*I* of 5.94 (blue arrow, t = 1000 s). The final GFP concentration was 4.13 mM, representing an enrichment factor of 413 times from the initial concentration (blue arrow, t = 3000 s). Two negative conductivity peaks (red arrow) appeared at ~100 s. While migrating toward the p*I*, the two negative conductivity peaks tracked the corresponding GFP peaks and merged into a single peak (blue

arrows, t = 1000 and 3000 s), indicating that the focused protein yielded an appreciable conductivity peak (peak height = 0.797 mS/m, t = 3000 s).

To elucidate the evolution of the negative conductivity peak, the concentration profiles of GFP and neighboring CAs were examined, along with the conductivity around the GFP p*I* without GFP (Fig. 3a and c) and with GFP (Fig. 3b and d). Without GFP, the CAs near the p*I* showed symmetric trapezoidal shapes featuring Gaussian legs. However, when GFP was focused, the concentrations of CA 20 and 21 were reduced in the order of those closest to the GFP peak. The CA profiles became asymmetric, tilting toward GFP (observed more clearly in Fig. 3d). The major cause for this distortion was that the CAs were "replaced" disproportionally by the focused GFP to maintain electroneutrality (Eq. S-8, S.D.) and constant-current conditions. GFP, which consists of 238 amino acid residues, is significantly larger and has a higher number of ionizable microforms than the CAs used in the simulation (maximum valence p_i = 37, n_i = −46 vs. p_i = 1, n_i = −1) [56]. Therefore, the charge number per molecule (i.e., net charge concentration divided by analytical concentration, see Eq. S-13) of GFP should be much larger than those of the CAs. In contrast, the CAs have much higher base mobility (i.e., $|z| = 1.30 \times 10^{-9}$ vs. 1.96×10^{-9} $m^2/V \cdot s$). Therefore, the effective mobility [56] of the CAs is much higher than that of GFP.

As the current is equal everywhere in the microchannel, the electric field should increase to compensate for the low effective mobility of GFP around its p*I*. Simultaneously, the CAs are reduced disproportionally (i.e., expelled) to compensate for the rapidly increasing local charge resulting from the focused GFP. The reduction of the CAs occurred by locally increasing electrophoretic velocity, induced by the increased electric field. In this manner, the concentrations of both GFP and CAs are adjusted to maintain electroneutrality and constant-current conditions. Consequently, the local conductivity, a combined contribution of GFP and CAs, reduces as the charge-carrying capability (i.e., charge × mobility × concentration) of GFP is lower. This reduced local conductivity manifests as "negative peaks" in Fig. 2d. The disproportional reduction in the CA concentrations was further investigated by examining the CAs near the GFP p*I*. In Fig. 3c, without GFP (0 mM) at ~3000 s, concentrations of CA 20 and 21 were 14.247 mM (red arrow) and 1.445 mM (blue arrow), respectively, while the conductivity was 17.725 mS/m, −52 μm from the GFP peak center (dotted vertical line). In the presence of focused GFP (4.134 mM), the concentrations of CA 20 and 21 were reduced to 12.148 mM (−14.7%, red arrow) and 1.123 mM (−22.3%, blue arrow) in Fig. 3d. The conductivity was reduced to 16.36 mS/m (−7.73%) because of the increased GFP concentration (low charge-carrying capability) and decreased CA concentrations (high charge-carrying capability). The charge numbers per molecule (Eq. S-13) for the CA 20, 21, and GFP were −0.0211, 0.0629 and −0.1296, respectively. Considering that the GFP is close to its p*I* (only 52 μm away), the charge number per molecule was significant, causing the disproportional CA replacement.

The physicochemical properties of the protein and their impacts on the height of the negative conductivity peaks were also investigated. Based on the peak-evolution mechanism, it was hypothesized that higher concentrations, lower mobility, and higher charges should increase the peak height assuming the other conditions are fixed (e.g., CA species, CA concentration, and electric field). To test this hypothesis, numerical simulations were performed using various GFP concentration, mobility, and charge conditions (see Section S.3.4 in the S.D. for further details). As shown in Fig. 4, the peak height, which corresponds to analytical sensitivity, was enhanced with higher concentrations (also shown experimentally in Section 3.4), smaller base mobility (i.e., larger molecular mass), and higher charge (i.e., more ionizable amino-acid residues). This may represent a new approach for improving the analytical sensitivity of protein C4D detection.

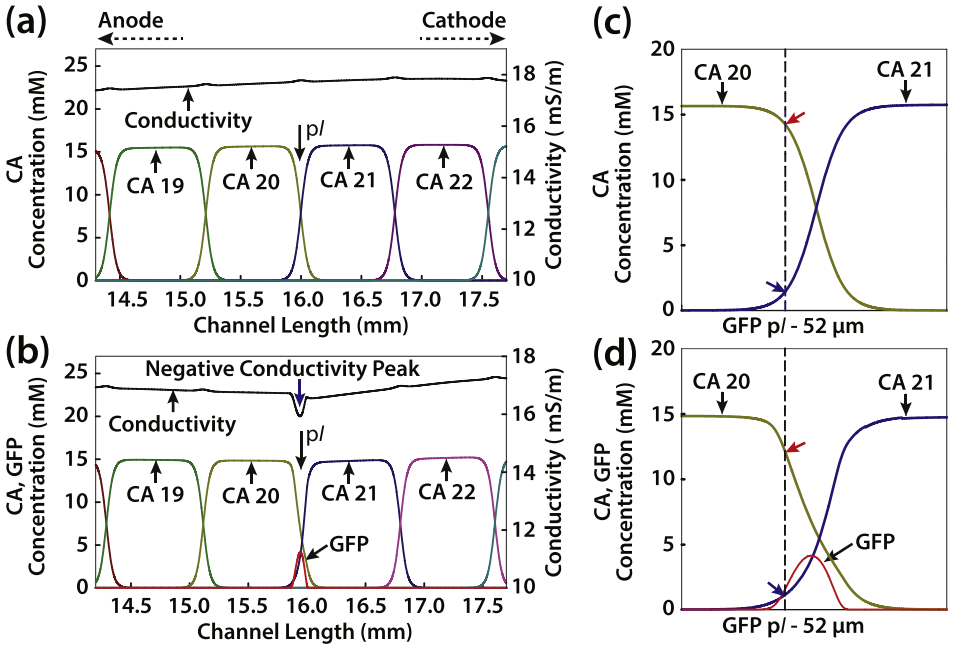

Fig. 3. Distributions of conductivity, CAs, and GFP around the GFP p*I* at 3000 s. (a) Without GFP, the CAs are distributed uniformly with symmetric trapezoidal shapes featuring Gaussian legs. (b) In the presence of GFP, distortion of the concentration profiles of CA 20 and 21 was observed, tilting toward the GFP peak. The focused GFP replaces the CAs (better charge-carrying) disproportionally to maintain charge neutrality and constant-current conditions, eventually lowering the local conductivity and yielding a negative conductivity peak. (c) Magnified view of (a). (d) Magnification of (b) near the GFP p*I* (distortion of the CA-peak shapes can be more clearly observed here). Both dotted vertical lines denotes −52 μm from the GFP p*I*.

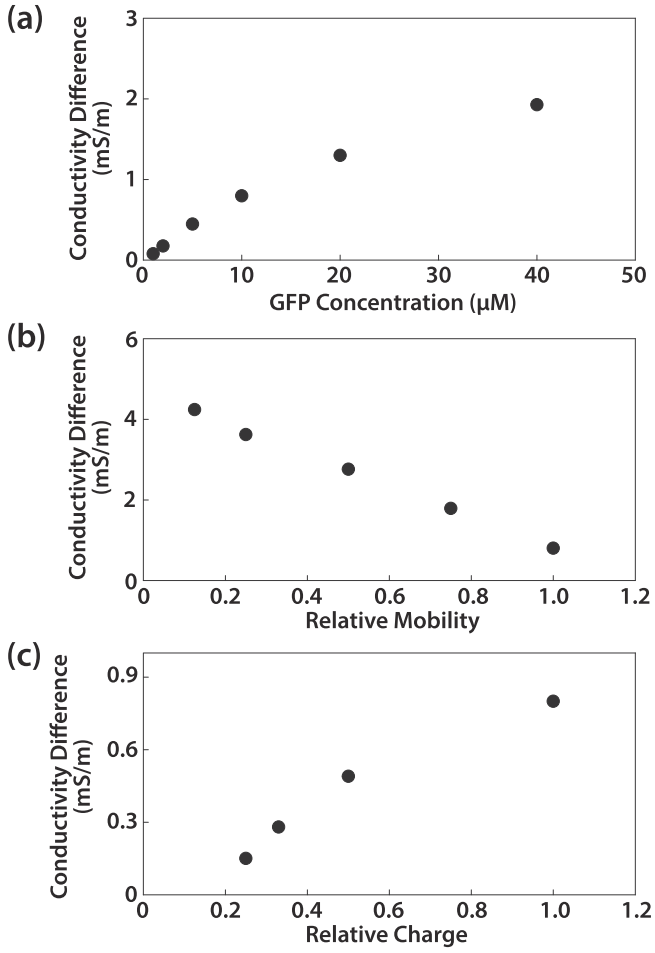

Fig. 4. Effects of three physicochemical properties of GFP on the height of negative conductivity peaks. (a) Simulation repeated with varying GFP concentrations (1, 2, 5, 10, 20, and 40 μM). The intensity of the negative conductivity peak increased with increasing concentration. (b) Simulation performed using reduced base mobility of protein (0.98, 0.49, 0.25, and 0.125 × 10^{-9} $m^2/V \cdot s$). The conductivity peak height increased with decreasing protein mobility. (c) Simulation performed using different numbers of ionizable residues, which were reduced to a half, a third, and a quarter of that of the avGFP. The conductivity-peak height decreased with decreasing protein charge.

3.2. Optimization of the mobilization conditions and study of pH-gradient stability

Slow pressure mobilization may prolong analysis time, while rapid mobilization may degrade separation resolution due to Taylor-Aris dispersion [50]. Therefore, the pressure mobilization conditions were experimentally optimized. As described in Section 2.4, 10 μL of the catholyte solution was removed for mobilization to ensure sufficient catholyte remained to stabilize pH, especially at the alkaline end. A 4% HEC concentration was chosen for all experiments because if a lower concentration (i.e., 3%) was used, significant peak broadening was observed (35.58% wider, compared to that obtained with 4% HEC), which is undesirable due to reduced sensitivity and resolution. In contrast, a higher HEC concentration (i.e., 5%) retarded mobilization speed by a factor of 2.67 compared to that achieved with 4% HEC. Pipetting out 10 μL of the catholyte and having 4% HEC in the separation medium were the optimal conditions for assay performance.

The focused CA species at the high pH region (pH 6.2–6.5) entered the cathode reservoir after mobilization and was mixed with the alkaline catholyte (pH 12.43). The loss of the high pH region may perturb the pH gradient during mobilization, which could affect the separation resolution of the focused protein bands. Therefore, a stability study of the pH gradient was essential. Pressure mobilization was performed using the optimized conditions, as described above. Fig. 5a shows the separation montage of mobilized p*I* markers at different time points. The p*I*-marker positions and estimated pH gradient are shown in Fig. 5b. The slope of the pH gradient remained practically constant during the investigated time (4 min) with a relative standard deviation (RSD) of 0.8%. In addition, the p*I*-marker bands were not further dispersed during migration. From these results, it can be concluded that the pH gradient was sufficiently stable to allow the μCIEF-C4D assay under the optimized pressure-mobilization conditions.

3.3. Confirmation of the μCIEF-C4D assay

We first tested CAs of a wide pH range (i.e., Pharmalyte pH 3–10) which worked well for previous protein focusing. However, combining the C4D with the μCIEF was immensely challenging; unidentifiable "ghost" conductivity peaks that did not originate from proteins were consistently observed because the peaks were not detected by fluorescence. Moreover, the conductivity peaks were sometimes overshadowed by significant baseline drift. The ghost peaks and baseline drift were likely due to parabolic-shaped, non-uniform background conductivity profile of the focused CAs, as previously reported [44]. For example, Pharmalytes (pH 3–10) yielded a parabolic-shaped conductivity profile, with minima at approximately pH 5.5–6.5 [44]. The origin of the non-uniform conductivity is somewhat unclear but is likely caused by the lack of appropriate p*K* values of the polyamine in this region [57]. Interestingly, CAs with a narrow pH range, for instance, Ampholine pH 3–6 (LKB Produkter AB, Bromma, Sweden) showed a relatively uniform conductivity profile [58]. Herein, Pharmalyte pH 4–6.5 yielded better results with fewer ghost peaks and significantly less baseline drift. Therefore, this Pharmalyte mixture was used in all experiments.

To determine if the C4D signal originated from the protein and was not a ghost peak, GFP focused using Pharmalyte pH 4–6.5 was co-

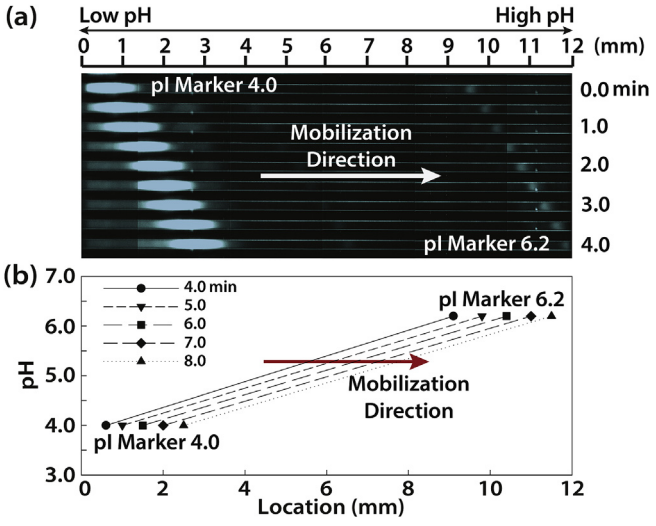

Fig. 5. Stability test of pH gradient during mobilization. (a) Separation montage of fluorescent p*I* markers at different time points after initiation of pressure mobilization. The fluorescent images were taken every 30 s. IEF conditions: standard separation medium of 2% CA + 4% HEC +5% CHAPS with 0.05-mg/mL fluorescent p*I* markers (p*I* 4.0 and 6.2), catholyte solution of 35 mM NaOH + 2% HEC, anolyte solution of 35 mM H_3PO_4 + 2% HEC, and separation electric field of 55.6 V/cm. (b) Time-sequence plot of the pH gradient obtained based on the location of the two p*I* markers. The pH-gradient slope was stable during mobilization (RSD = 0.8%).

detected with fluorescence imaging. GFP was chosen as a model protein because it can be observed via conductivity and fluorescent signals without fluorescence labeling. As shown in Fig. 6, both C4D and fluorescence peaks were concurrently detected while the focused GFP band passed the gap of the C4D-electrode pair (i.e., detection point). Entering (3.0 min) and leaving (7.0 min) the electrode gap were fluorescently captured (Fig. 6a). The obtained C4D and fluorescence signals of the 10-μM GFP-F64L variant were co-plotted in Fig. 6b. The rise and fall of the positive fluorescence peak coincided with the fall and rise of the negative conductivity peak, respectively. This confirmed that the detected conductivity peak could be attributed to the actual GFP band and was not a ghost peak.

3.4. Quantitation of GFP using the μCIEF-C4D assay

After the μCIEF-C4D was confirmed using fluorescence co-detection, quantitative measurement of GFP was performed (i.e., F64L variant). Representative conductometric electropherograms for a blank solution (broken line) and 30 μM GFP (solid line) are shown in Fig. 7a. Because of the non-flat conductivity profile of the focused CAs, baseline drift was observed. However, the drift was 8.6 times less (22.92 mV/min, $n = 5$) compared to that obtained with Pharmalyte pH 3–10 cases (197.77 mV/min, $n = 5$) and an apparent negative conductivity peak (57.98 mV) was obtained after the baseline correction.

GFP over a wide concentration range (10 nM–35 μM) was focused, mobilized, and detected using our μCIEF-C4D assay. Fig. 7b shows the conductivity curves obtained at different concentrations after baseline correction. The shapes of the conductivity peaks were not Gaussian at low concentrations (10 nM–2 μM) because two closely-spaced GFP isoforms (a major peak and a minor peak observed in fluorescence images) were merged and not resolved due to dispersion during pressure mobilization. It should be noted

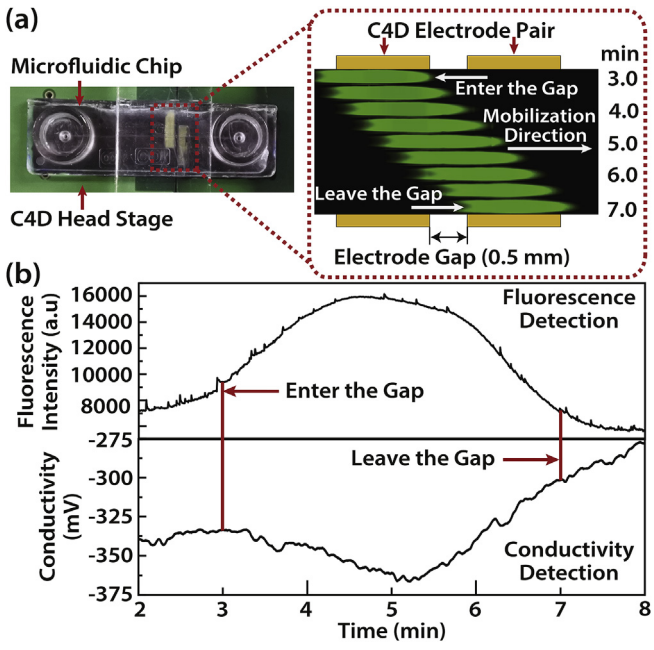

Fig. 6. Confirmation of μCIEF-C4D protein detection. (a) Migration montage of a GFP band over the C4D-electrode gap obtained every 30 s for 4 min after mobilization. The GFP concentration was 10 μM. Other IEF conditions were identical to those described in Fig. 5. (b) Conductivity and fluorescence signals simultaneously measured at the C4D electrode gap. The negative conductivity peak and positive fluorescence peak coincided. C4D conditions: excitation frequency = 300 kHz; excitation voltage = 200 V; and headstage gain on for boosting the conductivity signal.

that the mobilization direction of 1-μM GFP was reversed, and the major peak appeared first. At high concentrations (>2 μM), the peak shape became Gaussian as the minor peak was overwhelmed by the major peak. The peak height increased until a GFP concentration of 30 μM. The conductivity signal for 35-μM GFP was smaller than that of 30-μM GFP (i.e., 13.61 vs. 57.98 mV). The reduction of conductivity was likely due to protein precipitation we observed (Fig. S10, S.D.). Initially, 4% CHAPS was used for all experiments, but precipitation was observed at 30-μM GFP. Therefore, the CHAPS concentration was increased to 5% to solubilize the focused 30-μM GFP. However, precipitation still occurred for 35 μM GFP even at this high CHAPS concentration.

A calibration curve was generated using a logistic curve ($R^2 = 0.989$), as presented in Fig. 7c. Peak height was used for quantitation of IEF-focused proteins, and the relation between the peak height and protein concentration showed a similar response as observed in the literature [59]. The peak height of a focused protein is expected to be proportional to concentration but inversely proportional to the cube of peak width, as described by Eq. (6) in Ref. (46). As the focused GFP reduces CAs around its p*I*, the local pH gradient formed by the CAs is established such that the gradient slope is lower at higher GFP concentrations (as confirmed by our simulation). Therefore, the GFP peak disperses more at higher GFP concentrations as electromigration toward the peak center weakens, which may cause increased peak width. This is likely the origin of the deviation from a linear response at higher concentrations and consequently the reason underlying the "logistic" calibration curve. The LOD was determined to be 10 nM (signal-to-noise ratio = 3) using the peak height and standard deviation of noise measured at the C4D-signal baseline (25 data points). Optical (UV and fluorescence) detection for μCIEF yielded a LOD of 0.7–1.8 nM [19,60]. Our fluorescence detection estimated the LOD to be ~0.3 nM (see Section S.6 in the S.D. for further details). In contrast, the LOD of a typical C4D detection for zone electrophoresis is 35–141 nM [61]. Therefore, the 10-nM LOD of our MIF-C4D is remarkable. Moreover, as a label-free detection technique, complicated and tedious fluorescence labeling, which can increase protein heterogeneity and hydrophobicity, is not required. When combining the enrichment capability of IEF and optimized C4D conditions, clinically relevant protein concentrations can be measured (e.g., total PSA concentration is 27.8 nM in metastatic prostate cancer diagnoses [16]). The reproducibility of the C4D measurement was also determined using 100 nM GFP, and the RSD of the peak height was excellent (2.53%; see Section S.7 in the S.D. for further details).

3.5. Multiple protein analysis

Multiple resolved analytes have been detected using μCIEF [1,62]. The separation resolution (R_s) of IEF is expressed as ΔpH, the minimum-resolvable pH difference between two neighboring proteins [2]. A previously reported separation resolution for μCIEF with fluorescence detection was as good as 0.10 pH units [3]. The separation resolution of optical detection is limited by the pixel size of an image sensor [63] (e.g., on the order of a few μm for a scientific CCD sensor [64]) or pinhole size [65] (e.g., on the order of ~50 μm for PMT detection [64]). For conductometric detection, the gap between an electrode pair will ultimately limit the separation resolution. The gap between the C4D electrodes is relatively large (0.5–2.5 mm) [31] to minimize parasitic coupling between the two electrodes [66]. A large gap would deteriorate separation resolution. Many electrophoresis techniques have been combined with single-point detection so mobilization is inevitable for detection and causes band dispersion (e.g., Taylor-Aris dispersion). Consequently, achieving a high R_s value in μCIEF-C4D methods can be

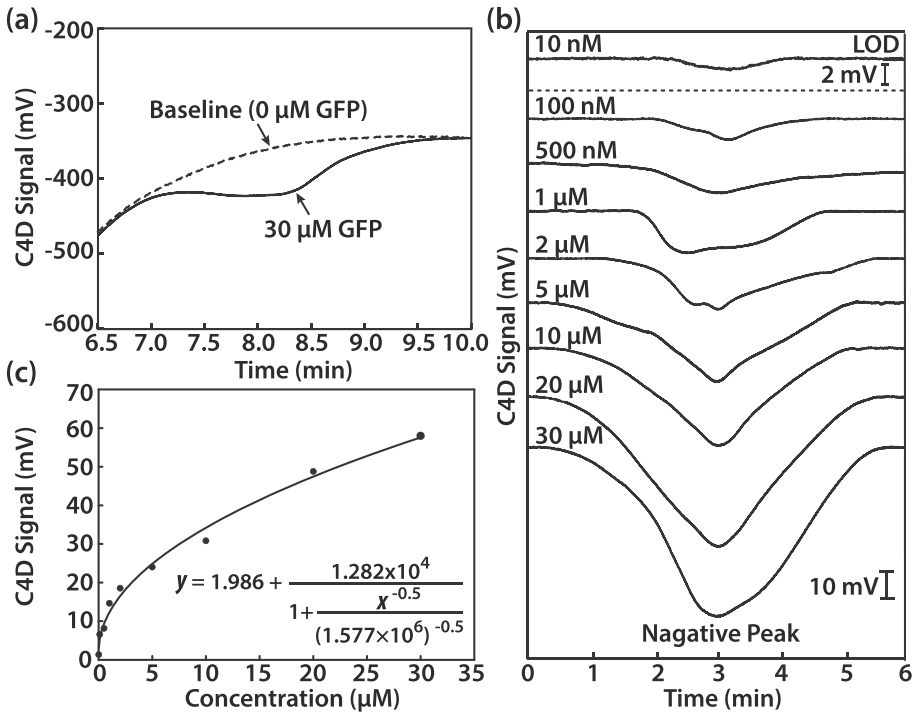

Fig. 7. Quantitation of GFP using our μCIEF-C4D assay. (a) Electropherogram for a blank separation medium (0 μM GFP, broken line) and the same medium containing 30 μM GFP (solid line). A clear negative peak of 57.98 mV was observed. The IEF and C4D conditions were identical to those shown in Fig. 6 (b) Conductivity peaks detected at different GFP concentrations after the baseline correction. Based on a signal-to-noise ratio of 3, the LOD was estimated to be 10 nM. (c) Calibration curve for the C4D signal (peak height) as a function of GFP concentration obtained using a logistic function ($R^2 = 0.989$) with a detection range of 10 nM–30 μM.

challenging. Therefore, the separation capability of the μCIEF-C4D method was examined using multiple fluorescent proteins (Fig. 8).

The fluorescence proteins RK-GFP, GFP-F64L, and R-PE were chosen as they have similar p*I* values. The measured p*I* values of RK-GFP, GFP-F64L, and R-PE were 6.02, 5.48, and 5.01, respectively (Fig. 8a). For fluorescence imaging, the R_s between RK-GFP and GFP-F64L was 3.59, while it was 4.55 between GFP-F64L and R-PE. For C4D detection, a mixture of RK-GFP (5 μM), GFP-F64L (5 μM), and R-PE (1 μM) was used (Fig. 8b). After the proteins were separated and focused (~4 min), all the focused-protein bands were pressure-mobilized in the cathode direction. As the three protein bands passed the electrode gap (i.e., between the two red lines in Fig. 8b), the fluorescence and conductivity signals were concurrently recorded. Conductometric electropherograms for GFP-F64L, RK-GFP, and R-PE are shown from three consecutive runs (Fig. 8c). Our μCIEF-C4D assay separated and detected multiple proteins. The average R_s between the RK-GFP and GFP-F64L was 2.07, equivalent to a ΔpH of 0.47. The average R_s between GFP-F64L and R-PE was 2.06, equivalent a ΔpH of 0.54. Thus, two different proteins or isoforms with a minimum p*I* difference of 0.25 pH units can be resolved (see Section S.8 in the S.D. for detailed calculations). This result is remarkable considering the broad C4D-electrode gap (0.5 mm) and dispersion during pressure mobilization. Currently, further optimization of the experimental conditions are ongoing to maximize R_s, namely the type and concentration of polymer solution (e.g., HEC), electric field during mobilization, and amount of aspired catholyte. Adopting a shorter electrode gap while reducing parasitic coupling using a Faraday shield may also improve the R_s [28].

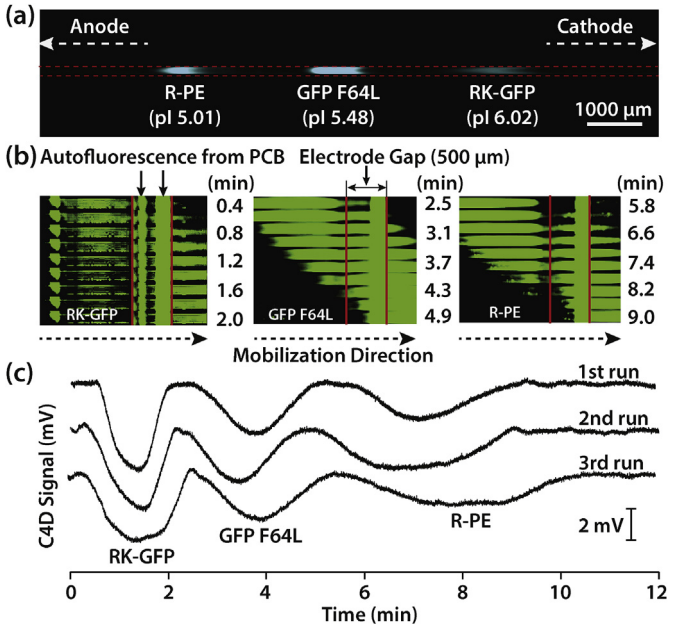

Fig 8. μCIEF-C4D detection of multiple proteins. (a) Separation image of the fluorescence proteins, RK-GFP (1.2 μM), GFP-F64L (1 μM), and R-PE (0.1 μM) taken after isoelectric focusing for p*I* determination. (b) Migration of the three proteins in the following order: RK-GFP (5 μM), GFP-F64L (5 μM), and R-PE (1 μM) over the C4D electrode. (c) Corresponding electropherograms for three consecutive runs. The separation medium and IEF conditions were identical to those described in Fig. 7.

4. Conclusions

We noticed the potential of a highly portable μCIEF system and the benefits of electronics-only, universal, and contactless conductivity detection. Therefore. C4D was applied in μCIEF for a potentially portable analytical system. For the rational design of the

μCIEF-C4D assay, the fundamental mechanism of the evolution of the negative conductivity peak of a focused protein was elucidated using numerical simulations.

We successfully demonstrated the feasibility of the newly developed μCIEF-C4D assay for "label-free" protein analysis by overcoming diverse analytical challenges. Regardless of the non-uniform background conductivity profiles of the focused CAs, we confirmed that the negative conductivity peak originated from the real, focused GFP using fluorescence co-detection. GFP was detected over a wide concentration range from 10 nM to 30 μM. The LOD was surprisingly low (10 nM) considering that C4D is an indirect (i.e., capacitively coupled) conductometric method. The LOD for the μCIEF fluorescence detection is better, on the order of a few hundred pM [19]. However, complicated and tedious fluorescence labeling is often difficult, and bulky and power-consuming optical instrumentation is required for analysis. The μCIEF-C4D assay result for multiple fluorescent proteins indicates that it can detect proteins with a minimum p*I* difference of 0.25 pH units. This result is remarkable considering that the gap between the two C4D electrodes is large (0.5 mm) and pressure-mobilization induces band dispersion. Additionally, a total analysis time for all proteins took only ~12 min.

Currently, the IEF simulation is being enhanced by including additional parameters (i.e., the number and concentration of CAs). Further optimization of the assay in on-going to improve separation resolution, expand the workable pH range, and analyze non-fluorescent proteins of diagnostic significance. We foresee that a μCIEF-C4D-based, highly portable analysis system could be realized in the near future.

Declaration of competing interest

The authors declare that they have no known competing financial interests or personal relationships that could have appeared to influence the work reported in this paper.

CRediT authorship contribution statement

Minh Khang Chau: Writing - original draft, Investigation, Visualization, Data curation, Formal analysis, Validation. **Nebiyu Getachew Arega:** Investigation, Visualization. **Nguyen Anh Nhung Tran:** Resources. **Jin Song:** Investigation, Visualization. **Sangmin Lee:** Resources. **Jintae Kim:** Funding acquisition, Conceptualization, Supervision. **Minsub Chung:** Funding acquisition, Conceptualization, Resources, Supervision, Validation. **Dohyun Kim:** Writing - review & editing, Conceptualization, Methodology, Supervision, Project administration, Funding acquisition, Validation.

Acknowledgments

This work was supported by the Samsung Research Funding Center of Samsung Electronics under Project Number SRFC-IT1401-07. This research was also supported by the Basic Science Research Program through the National Research Foundation of Korea funded by the Ministry of Education, Science, and Technology (NRF-2016R1D1A1B03931842).

Appendix A. Supplementary data

Supplementary data to this article can be found online at https://doi.org/10.1016/j.aca.2020.05.028.

References

[1] X. Huang, J. Ren, On-line chemiluminescence detection for isoelectric focusing of heme proteins on microchips, Electrophoresis 26 (2005) 3595–3601.
[2] G.J. Sommer, A.V. Hatch, IEF in microfluidic devices, Electrophoresis 30 (2009) 742–757.
[3] C. Das, Z.H. Fan, Effects of separation length and voltage on isoelectric focusing in a plastic microfluidic device, Electrophoresis 27 (2006) 3619–3626.
[4] A.M. Tentori, A.J. Hughes, A.E. Herr, Microchamber integration unifies distinct separation modes for two-dimensional electrophoresis, Anal. Chem. 85 (2013) 4538–4545.
[5] S. Jeeawoody, K.A. Yamauchi, A. Su, A.E. Herr, Laterally aggregated polyacrylamide gels for immunoprobed isoelectric focusing, Anal. Chem. 92 (2020) 3180–3188.
[6] S. Mikkonen, J. Jacksén, J. Roeraade, W. Thormann, Å. Emmer, Microfluidic isoelectric focusing of amyloid beta peptides followed by micropillar-matrix-assisted laser desorption ionization-mass spectrometry, Anal. Chem. 88 (2016) 10044–10051.
[7] S. Mack, D. Arnold, G. Bogdan, L. Bousse, L. Danan, V. Dolnik, M. Ducusin, E. Gwerder, C. Herring, M. Jensen, J. Ji, S. Lacy, C. Richter, I. Walton, E. Gentalen, A novel microchip-based imaged CIEF-MS system for comprehensive characterization and identification of biopharmaceutical charge variants, Electrophoresis 40 (2019) 3084–3091.
[8] C. Herzog, E. Poehler, A.J. Peretzki, S.M. Borisov, D. Aigner, T. Mayr, S. Nagl, Continuous on-chip fluorescence labelling, free-flow isoelectric focusing and marker-free isoelectric point determination of proteins and peptides, Lab Chip 16 (2016) 1565–1572.
[9] S. Jezierski, D. Belder, S. Nagl, Microfluidic free-flow electrophoresis chips with an integrated fluorescent sensor layer for real time pH imaging in isoelectric focusing, Chem. Commun. 49 (2013) 904–906.
[10] G.J. Sommer, J. Mai, A.K. Singh, A.V. Hatch, Microscale isoelectric fractionation using photopolymerized membranes, Anal. Chem. 83 (2011) 3120–3125.
[11] G.J. Sommer, A.K. Singh, A.V. Hatch, On-chip isoelectric focusing using photopolymerized immobilized pH gradients, Anal. Chem. 80 (2008) 3327–3333.
[12] Y. Li, J.S. Buch, F. Rosenberger, D.L. DeVoe, C.S. Lee, Integration of isoelectric focusing with parallel sodium dodecyl sulfate gel electrophoresis for multidimensional protein separations in a plastic microfluidic network, Anal. Chem. 76 (2004) 742–748.
[13] Y.-C. Wang, M.H. Choi, J. Han, Two-dimensional protein separation with advanced sample and buffer isolation using microfluidic valves, Anal. Chem. 76 (2004) 4426–4431.
[14] S.Q. Tia, K. Brown, D. Chen, A.E. Herr, Protein post-translational modification analyses using on-chip immunoprobed isoelectric focusing, Anal. Chem. 85 (2013) 2882–2890.
[15] W. Tan, Z.H. Fan, C.X. Qiu, A.J. Ricco, I. Gibbons, Miniaturized capillary isoelectric focusing in plastic microfluidic devices, Electrophoresis 23 (2002) 3638–3645.
[16] A.J. Hughes, R.K.C. Lin, D.M. Peehl, A.E. Herr, Microfluidic integration for automated targeted proteomic assays, Proc. Natl. Acad. Sci. U.S.A. 109 (2012) 5972.
[17] W. Jang, J. Shim, D.-Y. Lee, P. Dutta, J.-R. Kim, K.-H. Cho, Rapid detection of dysfunctional high-density lipoproteins using isoelectric focusing-based microfluidic device to diagnose senescence-related disease, Electrophoresis 32 (2011) 3415–3423.
[18] A.J. Vickers, A.M. Cronin, G. Aus, C.-G. Pihl, C. Becker, K. Pettersson, P.T. Scardino, J. Hugosson, H. Lilja, A panel of kallikrein markers can reduce unnecessary biopsy for prostate cancer: data from the European Randomized Study of Prostate Cancer Screening in Göteborg, Sweden, BMC Med. 6 (2008) 19.
[19] C. Das, Z. Xia, A. Stoyanov, Z.H. Fan, A laser-induced fluorescence imaging system for isoelectric focusing, Instrum. Sci. Technol. 33 (2005) 379–389.
[20] D.P. Richards, C. Stathakis, R. Polakowski, H. Ahmadzadeh, N.J. Dovichi, Labeling effects on the isoelectric point of green fluorescent protein, J. Chromatogr. A 853 (1999) 21–25.
[21] L.C. Zanetti-Domingues, C.J. Tynan, D.J. Rolfe, D.T. Clarke, M. Martin-Fernandez, Hydrophobic fluorescent probes introduce artifacts into single molecule tracking experiments due to non-specific binding, PLoS One 8 (2013), e74200.
[22] M. Vlčková, F. Kalman, M.A. Schwarz, Pharmaceutical applications of isoelectric focusing on microchip with imaged UV detection, J. Chromatogr. A 1181 (2008) 145–152.
[23] A.J. Zemann, E. Schnell, D. Volgger, G.K. Bonn, Contactless conductivity detection for capillary electrophoresis, Anal. Chem. 70 (1998) 563–567.
[24] J.A. Fracassi da Silva, C.L. do Lago, An oscillometric detector for capillary electrophoresis, Anal. Chem. 70 (1998) 4339–4343.
[25] P. Kubáň, P.C. Hauser, Application of an external contactless conductivity detector for the analysis of beverages by microchip capillary electrophoresis, Electrophoresis 26 (2005) 3169–3178.
[26] L.T.D. Cappelini, P. de Fátima Menegoci Eugênio, P.A.G.C. Leão, J.V. Alberice, A.C. Urbaczek, N.A. Assunção, L. Juliano, E. Carrilho, Capillary electrophoresis coupled to contactless conductivity detection for analysis of amino acids of agricultural interest in composting, Electrophoresis 37 (2016) 2449–2457.
[27] J. Gorbatsova, M. Borissova, M. Kaljurand, Electrowetting on dielectric actuation of droplets with capillary electrophoretic zones for MALDI mass spectrometric analysis, Electrophoresis 33 (2012) 2682–2688.
[28] E.M. Abad-Villar, J. Tanyanyiwa, M.T. Fernández-Abedul, A. Costa-García, P.C. Hauser, Detection of human immunoglobulin in microchip and conventional capillary electrophoresis with contactless conductivity measurements, Anal. Chem. 76 (2004) 1282–1288.
[29] M. Stojkovic, N.R. Uda, P. Brodmann, M. Popovic, P.C. Hauser, Determination of

PCR products by CE with contactless conductivity detection, J. Separ. Sci. 35 (2012) 3509–3513.
[30] W.K.T. Coltro, R.S. Lima, T.P. Segato, E. Carrilho, D.P. de Jesus, C.L. do Lago, J.A.F. da Silva, Capacitively coupled contactless conductivity detection on microfluidic systems—ten years of development, Anal. Methods 4 (2012) 25–33.
[31] M. Pumera, Contactless conductivity detection for microfluidics: designs and applications, Talanta 74 (2007) 358–364.
[32] M. Pumera, J. Wang, F. Opekar, I. Jelínek, J. Feldman, H. Löwe, S. Hardt, Contactless conductivity detector for microchip capillary electrophoresis, Anal. Chem. 74 (2002) 1968–1971.
[33] M. Zhang, S.C. Phung, P. Smejkal, R.M. Guijt, M.C. Breadmore, Recent trends in capillary and micro-chip electrophoretic instrumentation for field-analysis, Trends Environ. Anal. Chem. 18 (2018) 1–10.
[34] A. Van Schepdael, Recent advances in portable analytical electromigration devices, Separations (2016) 3.
[35] H. Muhlberger, W. Hwang, A.E. Guber, V. Saile, W. Hoffmann, Polymer lab-on-a-chip system with electrical detection, IEEE Sensor. J. 8 (2008) 572–579.
[36] P.I. Koczka, E. Bodoki, A. Gáspár, Application of capacitively coupled contactless conductivity as an external detector for zone electrophoresis in poly(dimethylsiloxane) chips, Electrophoresis 37 (2016) 398–405.
[37] C. Huck, A. Poghossian, M. Bäcker, S. Chaudhuri, W. Zander, J. Schubert, V.K. Begoyan, V.V. Buniatyan, P. Wagner, M.J. Schöning, Capacitively coupled electrolyte-conductivity sensor based on high-k material of barium strontium titanate, Sensor. Actuators B Chem. 198 (2014) 102–109.
[38] P.I. Koczka, R. Bodor, M. Masár, A. Gáspár, Application of isotachophoresis in commercial capillary electrophoresis instrument using C4D and UV detection, Electrophoresis 37 (2016) 2384–2392.
[39] M. Novakova, L. Krivankova, M. Bartos, V. Urbanova, K. Vytras, Isotachophoretic determination of hydrosulfite and metabisulfite in technical samples, Talanta 74 (2007) 183–189.
[40] B.M. Koshel, M.J. Wirth, Trajectory of isoelectric focusing from gels to capillaries to immobilized gradients in capillaries, Proteomics 12 (2012) 2918–2926.
[41] P. Kubáň, P.C. Hauser, Contactless conductivity detection for analytical techniques: developments from 2016 to 2018, Electrophoresis 40 (2019) 124–139.
[42] P. Kubáň, P.C. Hauser, Contactless conductivity detection for analytical techniques— developments from 2014 to 2016, Electrophoresis 38 (2017) 95–114.
[43] A.V. Stoyanov, C. Das, C.K. Fredrickson, Z.H. Fan, Conductivity properties of carrier ampholyte pH gradients in isoelectric focusing, Electrophoresis 26 (2005) 473–479.
[44] W.J. Gelsema, C.L. De Ligny, N.G. Van Der Veen, Comparison of the specific conductivities, buffer, capacities and molecular weights of focused ampholine, servalyte and pharmalyte carrier ampholytes used in isoelectric focusing, J. Chromatogr. A 173 (1979) 33–41.
[45] W. Thormann, N.B. Egen, R.A. Mosher, M. Bier, Characterization of synthetic carrier ampholytes by repetitive scanning of the electric field during focusing, J. Biochem. Biophys. Methods 11 (1985) 287–293.
[46] R. Rodriguez-Diaz, M. Zhu, T. Wehr, Strategies to improve performance of capillary isoelectric focusing, J. Chromatogr. A 772 (1997) 145–160.
[47] S.-M. Chen, J.E. Wiktorowicz, Isoelectric focusing by free solutioncapillary electrophoresis, Anal. Biochem. 206 (1992) 84–90.
[48] A.M. Tentori, A.E. Herr, Performance implications of chemical mobilization after microchannel IEF, Electrophoresis 35 (2014) 1453–1460.
[49] S. Hjertén, J.-L. Liao, K. Yao, Theoretical and experimental study of high-performance electrophoretic mobilization of isoelectrically focused protein zones, J. Chromatogr. A 387 (1987) 127–138.
[50] M. Minárik, F. Groiss, B. Gaš, D. Blaas, E. Kenndler, Dispersion effects accompanying pressurized zone mobilisation in capillary isoelectric focusing of proteins, J. Chromatogr. A 738 (1996) 123–128.
[51] W.K.T. Coltro, J.A.F. da Silva, E. Carrilho, Fabrication and integration of planar electrodes for contactless conductivity detection on polyester-toner electrophoresis microchips, Electrophoresis 29 (2008) 2260–2265.
[52] J. Zhang, C. Das, Z.H. Fan, Dynamic coating for protein separation in cyclic olefin copolymer microfluidic devices, Microfluid. Nanofluidics 5 (2008) 327–335.
[53] A. Persat, R.D. Chambers, J.G. Santiago, Basic principles of electrolyte chemistry for microfluidic electrokinetics. Part I: acid–base equilibria and pH buffers, Lab Chip 9 (2009) 2437–2453.
[54] V. Hruška, M. Jaroš, B. Gaš, Simul 5 – free dynamic simulator of electrophoresis, Electrophoresis 27 (2006) 984–991.
[55] M. Bier, R.A. Mosher, O.A. Palusinski, Computer simulation and experimental validation of isoelectric focusing in ampholine-free systems, J. Chromatogr. A 211 (1981) 313–335.
[56] A. Persat, M.E. Suss, J.G. Santiago, Basic principles of electrolyte chemistry for microfluidic electrokinetics. Part II: coupling between ion mobility, electrolysis, and acid–base equilibria, Lab Chip 9 (2009) 2454–2469.
[57] P.G. Righetti, L. Balzarini, E. Gianazza, O. Brenna, Itaconic acid carrier ampholytes for isoelectric focusing, J. Chromatogr. A 134 (1977) 279–284.
[58] P.G. Righetti, Chapter 1 Theory and fundamental aspects of isoelectric focusing, in: T.S. Work, E. Work (Eds.), Laboratory Techniques in Biochemistry and Molecular Biology, Elsevier Biomedical Press, Amsterdam, 1983, pp. 1–86.
[59] J. Wu, J. Pawliszyn, Capillary isoelectric focusing with a universal concentration gradient imaging system using a charge-coupled photodiode array, Anal. Chem. 64 (1992) 2934–2941.
[60] Q. Mao, J. Pawliszyn, Demonstration of isoelectric focusing on an etched quartz chip with UV absorption imaging detection, Analyst 124 (1999) 637–641.
[61] J. Tursen, A. Wang, W. Qin, Electrophoretic separation of acidic and basic proteins in the presence of micromolar concentrations of an ionic liquid, Microchim. Acta 174 (2011) 63–71.
[62] J.C. Sanders, Z. Huang, J.P. Landers, Acousto-optical deflection-based whole channel scanning for microchip isoelectric focusing with laser-induced fluorescence detection, Lab Chip 1 (2001) 167–172.
[63] W. Bishara, T.W. Su, A.F. Coskun, A. Ozcan, Lensfree on-chip microscopy over a wide field-of-view using pixel super-resolution, Opt. Express 18 (2010) 11181–11191.
[64] E. Sánchez-Ortiga, C.J.R. Sheppard, G. Saavedra, M. Martínez-Corral, A. Doblas, A. Calatayud, Subtractive imaging in confocal scanning microscopy using a CCD camera as a detector, Opt. Lett. 37 (2012) 1280–1282.
[65] T. Wilson, Resolution and optical sectioning in the confocal microscope, J. Microsc. 244 (2011) 113–121.
[66] J.G.A. Brito-Neto, J.A. Fracassida Silva, L. Blanes, C.L. do Lago, Understanding capacitively coupled contactless conductivity detection in capillary and microchip electrophoresis. Part 1. fundamentals, Electroanalysis 17 (2005) 1198–1206.